Draft version August 31, 2026
Typeset using LaTeX twocolumn style in AASTeX7.0.1

Searching for Semi-relativistic Hypervelocity Stars with the *Euclid* and *Roman* Space Telescopes

James Guillochon[1] and Abraham Loeb[2]

[1] *Gentleman Astrophysicist*
[2] *Astronomy Department, Harvard University, 60 Garden Street, Cambridge, MA 02138, USA*

ABSTRACT

In 2015 we predicted that mergers of massive black hole (MBH) binaries launch stars into intergalactic space at 10^4–$10^5\,\mathrm{km\,s^{-1}}$ (≈ 0.03–$0.3c$), and that hundreds of these semi-relativistic hypervelocity stars (SHS) would be detectable in infrared surveys. No searches so far have revealed any such stars. We revisit the prediction in light of two developments. First, $e \gtrsim 0.5$ during hardening is now well-established by simulations: circumbinary disks settle at $e_{\rm eq} \simeq 0.45$–0.5 rather than circularizing, while retrograde disks pump toward $e \sim 1$. Pulsar timing arrays prefer a low-frequency turnover from environmental coupling, of which stellar slingshots are one leading interpretation. Second, the ejection speed depends almost entirely on the periapse, $v_\infty \propto (r_p/r_{\rm g,1})^{-1/2}$, independent of primary mass except as limited by tides. At fixed semimajor axis, $e = 0.5$ raises v_∞ by $\sqrt{2}$; $e = 0.9$ by $\sqrt{10}$. *Euclid* and *Roman* both provide near-infrared imaging that yields photometric candidates, and slitless grism spectroscopy that verifies the bright tail. *Euclid*'s Wide Survey yields ≈ 140 photometric detections at $H \simeq 24$ over 14,000 deg^2; *Roman*'s High-Latitude Wide-Area Survey goes deeper, yielding 10^2–10^3. Continuum detections in the two grisms are ≈ 0.3 at *Euclid* $H = 19.5$ and ≈ 0.4 at *Roman* $m_{\rm AB} \approx 21$; a velocity from bandheads is typically 0.5–1 mag brighter, so the completed surveys yield of order 0.1–0.5. A 5σ Rubin proper motion in r with a *Roman* photometric distance reaches ≈ 0.4 objects on the HLWAS footprint. A blueshifted photospheric spectrum would verify an SHS; a proper motion large for that distance, with no parallax, would solidify the identification.

Keywords: Hypervelocity stars (776) — Supermassive black holes (1663) — Galaxy mergers (608) — Intergalactic medium (813) — Sky surveys (1464)

1. INTRODUCTION

Stars ejected by the Hills (J. G. Hills 1988) mechanism from the Galactic center reach speeds of a few hundred to $\sim$1700 km s^{-1} (W. R. Brown et al. 2005; W. R. Brown 2015; S. E. Koposov et al. 2020). In A. Loeb & J. Guillochon (2014) and J. Guillochon & A. Loeb (2015, hereafter GL15) we pointed out that replacing the single massive black hole with a *merging* MBH binary removes the limitation that sets this ceiling. A star bound to the secondary is stripped when the secondary's Hill sphere shrinks below its orbital separation; if the binary is eccentric, the last stars to be released are those most tightly bound, and they leave with asymptotic speeds v_∞ that can exceed $10^4\,\mathrm{km\,s^{-1}}$ ($\approx 0.03c$) and in principle approach $c/2$. Because no other astrophysical channel produces unbound stars above $\approx 2.4\times10^4\,\mathrm{km\,s^{-1}}$ (R. Sari et al. 2010; I. Ginsburg et al. 2012), the detection of even one such object would be a direct diagnostic of an eccentric MBH merger.

We estimated that $\sim 10^6$ objects with $v_\infty > 10^4\,\mathrm{km\,s^{-1}}$ lie within the distance to the Virgo cluster, that roughly one SHS per 100 deg^2 would be detectable in a survey reaching $K = 24$, and that a next-generation wide-field infrared mission would yield tens to hundreds of detections. No searches so far have revealed any such stars.

Euclid is mapping $\sim$14,000 deg^2 over a six-year survey with slitless near-infrared spectroscopy (Euclid Collaboration & Y. Mellier 2025); the *Nancy Grace Roman Space Telescope* launched 2026 August 30; the Vera C. Rubin Observatory began its survey in 2026 June and has no astrometric baseline; *Gaia* DR4 has not yet been released.

The purpose of this paper is to make the case that the search should now be performed, and to specify how candidates can be *verified*. In §2 we restate the ejection kinematics of GL15 in abbreviated form, reducing them to a single scaling in the binary periapse and quantifying

Corresponding author: James Guillochon
Email: guillochon@gmail.com

the effect of eccentricity on v_∞ and on counts. In §3 we review the evidence, accumulated since 2015, that MBH binaries are eccentric during the phase that matters. In §4 we explain why the Galactic hypervelocity star null results do not constrain this population. In §5 we give a concrete search: photometric detections in *Euclid* and *Roman* imaging, verified by a grism radial velocity, a Rubin or *Roman* proper motion, or both.

2. EJECTION SPEED IS SET BY THE PERIAPSE

We collect the ejection kinematics of GL15 into a single scaling with binary periapse, without repeating the scattering experiments. Let the primary and secondary MBHs have masses M_1 and M_2, with $q_{12} \equiv M_1/M_2 > 1$, and let the binary have semimajor axis a and eccentricity e_{12}, so that its periapse separation is $r_p = a(1-e_{12})$. Stars bound to the secondary are removed when their apoapse exceeds the secondary's Hill radius evaluated at binary periapse (GL15),

$$r_{H,e} = r_p \left(\frac{M_2}{3M_1}\right)^{1/3}. \quad (1)$$

A star released from $a_{23} \simeq r_{H,e}$ has orbital speed $v_{23} = (GM_2/a_{23})^{1/2}$ about the secondary and is ejected with $v_\infty \simeq 1.3\, q_{12}^{1/6} v_{23}$, where the numerical factor accounts for the motion of the secondary at the moment of escape (R. Sari et al. 2010). Combining these,

$$v_\infty \simeq 1.3 \times 3^{1/6}\, q_{12}^{-1/6}\, c \left(\frac{r_p}{r_{\rm g,1}}\right)^{-1/2}, \quad (2)$$

where $r_{\rm g,1} \equiv GM_1/c^2$. Equation (2) matches the mean $v_\infty/\langle v_{23}\rangle$ of the GL15 experiments, with large scatter from orientation and phase. Numerically,

$$v_\infty \simeq 0.19\, c \left(\frac{r_p}{30\, r_{\rm g,1}}\right)^{-1/2} \left(\frac{q_{12}}{10}\right)^{-1/6}. \quad (3)$$

Equation (3) has three immediate consequences. First, when the periapse is expressed in gravitational radii of the primary, v_∞ is *kinematically* independent of M_1: the same periapse in units of $r_{\rm g,1}$ yields the same ejection speed for a $10^7\, M_\odot$ and a $10^9\, M_\odot$ primary. The *accessible* range of $r_p/r_{\rm g,1}$ is not. For a solar-type star the tidal radius is $r_t/r_{\rm g,1} \approx 0.47\, (M_1/10^9\, M_\odot)^{-2/3}$. The star's closest approach to the primary is $r_p - a_{23} \approx 0.68\, r_p$ at $q_{12} = 10$, so the innermost bound circular orbit (IBCO; $4r_{\rm g,1}$ for Schwarzschild) lies outside r_t at that closest approach only for $M_1 \gtrsim 7\times 10^7\, M_\odot$. Below that, the star is disrupted before it can reach the periapse of the fastest ejections: at $M_1 = 10^7\, M_\odot$, $r_t \approx 10 r_{\rm g,1}$ and the ceiling is $v_\infty \approx 0.27c$, not $c/2$. An intact star at $r_p = 280 r_{\rm g,1}$ around the $4 \times 10^6\, M_\odot$ Galactic-center primary (GRAVITY Collaboration et al. 2026) lies outside $r_t/r_{\rm g,1} \approx 19$ at that mass, an empirical illustration of the same survival cut. Second, the dependence on mass ratio is extremely weak, $q_{12}^{-1/6}$, so that a factor of ten in q_{12} changes v_∞ by only 32%. The near-coincidence of the $c/2$ cap with the IBCO in Figure 1(a) is a property of $q_{12} = 10$; at $q_{12} = 1$ the $c/2$ speed is reached at $r_p \approx 10 r_{\rm g,1}$, outside the IBCO, so the two ceilings are independent and their ordering depends on q_{12}. At $r_p = 30 r_{\rm g,1}$ the star already orbits the secondary at $\approx 0.1c$, so the upper-left corner of Figure 1(a) is where the Newtonian treatment is least trustworthy; the $c/2$ cap is the numerical and special-relativistic ceiling of GL15, not a Newtonian limit. A prograde orbit about a rapidly spinning primary moves the IBCO inward toward $\sim r_{\rm g,1}$ (J. M. Bardeen et al. 1972), which would raise the kinematic ceiling. Third, once tidal survival is satisfied, v_∞ depends only on $r_p/r_{\rm g,1}$. Reaching $v_\infty > 10^4\,{\rm km\,s^{-1}}$ requires $r_p \lesssim 10^3 r_{\rm g,1}$; reaching $v_\infty > 2.4 \times 10^4\,{\rm km\,s^{-1}}$, above which no other channel operates (R. Sari et al. 2010; I. Ginsburg et al. 2012), requires $r_p \lesssim 200 r_{\rm g,1}$.

Eccentricity enters only through $r_p = a(1 - e_{12})$, but it enters multiplicatively with the hardening. At a fixed stage of binary evolution,

$$\frac{v_\infty(e_{12})}{v_\infty(0)} = (1 - e_{12})^{-1/2}, \quad (4)$$

so $e_{12} = 0.5$ raises the ejection speed by $\sqrt{2}$ and $e_{12} = 0.9$ by $\sqrt{10}$. Because the velocity distribution is steep, the effect on detectable counts is larger than this suggests. For the differential distribution $P(v_\infty) \propto v_\infty^{-2.5}$ of the MBH-scattering channel (A. Sesana et al. 2007; B. D. Sherwin et al. 2008) that GL15 found to describe the population at several thousand ${\rm km\,s^{-1}}$, the cumulative $N(>v_\infty) \propto v_\infty^{-1.5}$, so the number above any fixed threshold scales as

$$\frac{N(>v_\infty; e_{12})}{N(>v_\infty; 0)} = (1 - e_{12})^{-0.75}, \quad (5)$$

a factor of ≈ 1.7 at $e_{12} = 0.5$ and ≈ 6 at $e_{12} = 0.9$. This is a property of $P(v_\infty)$, not a multiplier to apply on top of the GL15 density, which already assumed $e_{12} \gtrsim 0.5$. GL15 found the slope to steepen at higher velocities, which would only increase these factors.

Figure 1(a) shows v_∞ as a function of e_{12} for three hardening stages, for $M_1 = 10^9\, M_\odot$ and $q_{12} = 10$. Curves are truncated where r_p falls inside the innermost bound circular orbit (J. M. Bardeen et al. 1972) and capped at the $c/2$ speed limit identified in GL15. The figure shows that a binary that has hardened to milliparsec separations reaches the merger-only velocity regime across the range of eccentricities now predicted at hardening.

3. THE ECCENTRIC-MERGER PREMISE HAS STRENGTHENED

In GL15, the requirement that a significant fraction of MBH binaries pass through a phase with $e_{12} \gtrsim 0.5$ was the single largest source of uncertainty in the predicted space density. At the time it rested on N-body simulations of unequal-mass binaries embedded in stellar cusps (H. Baumgardt et al. 2006; M. Iwasawa et al. 2011; F. M. Khan et al. 2012) (the gas-poor channel), while the gas-rich channel was less clear. Both now favor $e_{12} \gtrsim 0.5$ during hardening: stellar scattering still drives eccentricity growth (M. Iwasawa et al. 2011; F. M. Khan et al. 2012; A. Sesana 2010), and circumbinary disks evolve to $e_{\rm eq} \simeq 0.45$–0.5 (or higher if retrograde) rather than circularizing (D. J. Muñoz et al. 2019; J. Zrake et al. 2021; M. Siwek et al. 2023; C. Tiede & D. J. D'Orazio 2024).

3.1. *Gas does not circularize these binaries*

High-resolution hydrodynamic simulations of accreting binaries embedded in circumbinary disks now consistently find that the orbit evolves toward a nonzero *equilibrium* eccentricity rather than toward zero. J. Zrake et al. (2021) find $e_{\rm eq} \simeq 0.45$ for equal-mass binaries, with circularization only for orbits initialized at $e \lesssim 0.08$. M. Siwek et al. (2023), in the largest parameter survey performed to date, find that eccentricities evolve to steady-state values that increase with mass ratio and saturate at $e_{\rm eq} \simeq 0.5$, and that binaries at their steady-state eccentricity with $q_b \gtrsim 0.3$ continue to evolve toward coalescence. D. J. Muñoz et al. (2019) found eccentricity growth at $e = 0.1$ and damping at $e = 0.5$–0.6, the sign change that implies an attractor. C. Tiede & D. J. D'Orazio (2024) find that retrograde disks instead pump eccentricity at every value they simulated (0–0.8), with $\dot{e} > 0$ throughout and $e \to 1$ in ~ 20 Myr at Eddington accretion; such high eccentricities would only raise v_∞ and, if the merger is plunging, tighten the beaming that concentrates the local population toward a few sources. See D. Lai & D. J. Muñoz (2023) for a review.

Gas dynamics need not supply the extreme eccentricities of the fastest ejections. It does mean that gas-rich MBH binaries are now expected to arrive at the hardening phase eccentric, at values straddling the $e_{12} \gtrsim 0.5$ threshold we required, and to remain so while they harden.

3.2. *Stellar dynamics drives eccentricity growth*

The stellar-dynamical channel identified before 2015 remains in place. M. Iwasawa et al. (2011) showed that the secondary's eccentricity grows through the preferential ejection of stars co-rotating with the binary, with the growth halted only by the discreteness noise of the scattered stars; H. Baumgardt et al. (2006) and F. M. Khan et al. (2012) found efficient, eccentric coalescence in merging galaxies. Near-equal-mass binaries show only mild eccentricity growth (A. Sesana 2010), so the effect is strongest at intermediate mass ratios, which is the regime that Equation (3) shows to be most favorable, since $v_\infty \propto q_{12}^{-1/6}$ varies negligibly across it.

3.3. *Pulsar timing arrays see the ejection process itself*

The detection of a nanohertz stochastic gravitational-wave background (G. Agazie et al. 2023a) is consistent with a cosmological population of MBH binaries (G. Agazie et al. 2023b). More directly relevant here, the measured spectrum shows a preference for a turnover at the lowest observed frequencies, which is naturally produced if the binaries are hardened by environmental coupling before gravitational-wave emission takes over. Y. Chen et al. (2026) attribute this turnover specifically to the extraction of orbital energy by three-body slingshot ejection of stars.

The process that the pulsar timing array data appear to require (three-body stellar slingshots that extract orbital energy (Y. Chen et al. 2026; A. Sesana 2010)) is the same family of encounters that unbinds stars from merging MBH binaries. That is indirect evidence that MBH binaries eject stars while they harden, not a measurement of the SHS space density.

3.4. *A caveat on LISA-band eccentricities*

J. Zrake et al. (2021) predict that binaries entering the LISA band will retain only $e \simeq 10^{-3}$–10^{-2}. Gravitational-wave emission circularizes the orbit efficiently (P. C. Peters 1964), but it does so at separations far smaller than those at which stars are stripped from the secondary's Hill sphere. The eccentricity relevant to SHS production is that of the hardening phase at $\sim 10^{-3}$–10^{-1} pc (A. Sesana 2010; C. Tiede & D. J. D'Orazio 2024), not the residual eccentricity at merger. Low LISA-band eccentricities and high hardening-phase eccentricities are entirely compatible, and both are predicted by the same simulations.

4. GALACTIC NULL RESULTS DO NOT APPLY

The strongest empirical statements about hypervelocity star production come from *Gaia*. T. Marchetti et al. (2022) searched the ~ 34 million DR3 sources

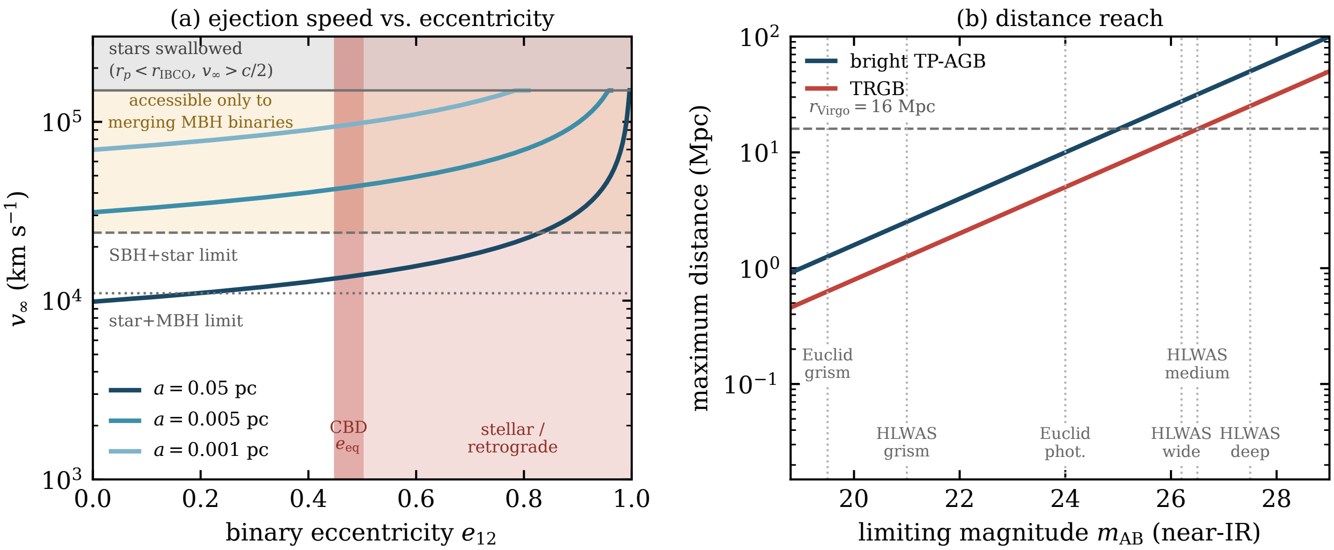

Figure 1. (a) Asymptotic ejection speed as a function of binary eccentricity for three hardening stages ($M_1 = 10^9\,M_\odot$, $q_{12} = 10$), from Equation (2). Curves terminate where the periapse reaches the innermost bound circular orbit (J. M. Bardeen et al. 1972) and are capped at $c/2$. At $q_{12} = 10$ those two limits nearly coincide; they are independent constraints whose ordering depends on mass ratio, and intact survival at the IBCO periapse requires $M_1 \gtrsim 7 \times 10^7\,M_\odot$ (see text). The dotted and dashed lines mark the Hills-mechanism ceilings derived in GL15 from the encounter kinematics of R. Sari et al. (2010): $1.1 \times 10^4\,{\rm km\,s^{-1}}$ for a stellar binary and a single MBH (consistent with I. Ginsburg et al. 2012), and $2.4 \times 10^4\,{\rm km\,s^{-1}}$ for a stellar-mass black hole–star binary. The shaded region above is accessible only to merging MBH binaries. The vertical band marks the range of eccentricities now predicted during hardening: the circumbinary-disk attractor $e_{\rm eq} \simeq 0.45$–0.5 (J. Zrake et al. 2021; M. Siwek et al. 2023; D. J. Muñoz et al. 2019), and the higher values reached by stellar scattering and retrograde disks (M. Iwasawa et al. 2011; F. M. Khan et al. 2012; C. Tiede & D. J. D'Orazio 2024). (b) Maximum distance at which a star of given absolute magnitude is detected as a function of limiting near-infrared magnitude, for two characteristic luminosities introduced here (the tip of the red giant branch and bright TP-AGB stars) rather than the mixed isochrone sample of GL15. *Euclid H* and *Roman* F158 are treated as equivalent AB magnitudes. Vertical lines mark the *Euclid* and HLWAS grism continuum limits, *Euclid*'s photometric depth (the limit assumed in GL15), and the HLWAS wide, medium, and deep tiers. The dashed horizontal line is the Virgo distance within which GL15 computed the population, a computational boundary rather than a physical one.

with full six-dimensional phase-space information and found no candidate above $700\,{\rm km\,s^{-1}}$ with reliable six-dimensional kinematics, deriving an ejection rate $\lesssim 8 \times 10^{-5}\,{\rm yr^{-1}}$. S. Verberne et al. (2024) identified 600 candidates, obtained ground-based follow-up for 196, found no new hypervelocity star, and constrained the ejection rate for stars above $1\,M_\odot$ to $< 10^{-5}\,{\rm yr^{-1}}$ at 2σ. F. A. Evans et al. (2023) used the absence of candidates to exclude a companion to Sgr A* more massive than $2000\,M_\odot$ within one milliparsec.

These do not bear on the SHS population, for three independent reasons:

Mechanism. T. Marchetti et al. (2022) and S. Verberne et al. (2024) model Hills ejection by a single MBH; F. A. Evans et al. (2023) consider a possible companion to Sgr A* but constrain it with the same Galactic hypervelocity-star sample. The SHS channel requires an MBH *merger*. The Milky Way is not undergoing one; indeed F. A. Evans et al. (2023) conclude that Sgr A* has had no companion more massive than $500\,M_\odot$ for at least 10 Myr, which is consistent with our framework.

Volume. The *Gaia* 6D sample is confined to the Galaxy. The SHS population is extragalactic, and in GL15 we speculated that if ejections are beamed, the local density may originate from a couple of mergers, illustrated with an event in M87. We predicted only $\sim 10^2$ objects with $v_\infty > 10^4\,{\rm km\,s^{-1}}$ within 1 Mpc of the Milky Way, and those are predominantly low-mass dwarfs requiring space-based depth.

Selection. A star moving at $10^4\,{\rm km\,s^{-1}}$ at a distance of 1 Mpc has a proper motion of 2.1 mas yr^{-1}; at 10 Mpc, 0.21 mas yr^{-1}. Searches that select on large proper motion combined with a measured radial velocity are blind to such objects by construction.

5. A CONCRETE SEARCH WITH *EUCLID* AND *ROMAN*

Both missions provide wide-field near-infrared imaging that yields photometric candidates, and slitless grism spectroscopy that can verify the bright tail kinematically.

Euclid's Wide Survey maps $\sim$14,000 deg^2 to $H \simeq 24$ with NISP slitless spectroscopy at $R \sim 450$ over 1.21–1.89 μm (Euclid Collaboration & Y. Mellier 2025), the Euclid-class limit assumed in GL15. That area is a six-year goal, not a current footprint: nominal survey operations began in 2024 February, 5000 deg^2 had been observed by 2026 March, and the Wide Survey completes around 2030. DR1 is scheduled for 2026 October.

The *Roman* High-Latitude Wide-Area Survey (HLWAS) covers $\approx$ 4900 deg^2 in three tiers (ROTAC): a wide tier of $\approx$ 2500 deg^2 reaching $m_{\rm AB} = 26.2$ in F158; a medium tier of $\approx$ 2350 deg^2 reaching 26.5 mag (AB) in three filters, with slitless grism spectroscopy over the same area; and a deep tier of 19.2 deg^2 (two fields of $\approx$ 9.5 deg^2) reaching about 1.1 mag deeper in F158 ($m_{\rm AB} \approx 27.5$), of which an ultra-deep component of $\approx$ 5.5 deg^2 reaches 28.2.[3] The wide-field instrument delivers a 0.28 deg^2 field at $0\farcs11$ pixels (R. Akeson et al. 2019), and the grism spans 1.0–1.93 μm at resolving power $R \approx$ 475–900 (E. Bray et al. 2024). The detection calculation below is the same for both surveys; only the area and depth change. We treat *Euclid* H and *Roman* F158 as equivalent AB magnitudes.

5.1. *Photometric detections are candidates*

Rescaling our surface density of one SHS per 100 deg^2 at the $H < 24$ Euclid- or WFIRST-class limit of GL15 (AB in the survey papers that set that cut; the introductory $K = 24$ is the same infrared depth), and splitting the detections as in GL15 (red-giant-branch stars about half; the brighter giant branches the rest), gives a Euclidean surface density that depends only on depth. We apply that density at *Euclid* H and *Roman* F158 with no $H - K$ offset. The circumbinary-disk attractor confirms the $e_{12} \gtrsim 0.5$ already assumed in GL15 rather than raising the counts; retrograde $e_{12} = 0.9$ can still sit a factor ≈ 6 above (Equation (5)). That normalisation is inherited from GL15 and is unrevised; merger-rate density, loss-cone supply, isochrone conversion, and the high-velocity slope of $P(v_\infty)$ each contribute uncertainties of order a dex or more, larger than the eccentricity envelope itself.

SHS are not sourced only within 16 Mpc. A star at $0.03c$ travels $\approx$ 130 Mpc in a Hubble time, so the local density is an integral over the merger history of a $\sim$ 100 Mpc sphere, and there is no physical reason for it to fall off outside Virgo. We therefore take Euclidean growth as the primary prediction, with the $r_{\rm Virgo}$ truncation of GL15 as a conservative floor. Applied to each survey (Figure 2): *Euclid*'s $H \simeq 24$ Wide Survey recovers the original GL15 forecast, $\approx$ 140 photometric detections over 14,000 deg^2. The HLWAS wide tier, 2.2 mag deeper, contains $\approx$ 530; the medium tier, 0.3 mag deeper still, $\approx$ 750; the 19.2 deg^2 deep tier, 1.1 mag deeper in F158, $\approx$ 24 rather than the $\approx$ 4 at which the truncated calculation saturates, an order-of-magnitude increase, which is why we develop the photometric selection there (§6).

These are faint red point sources, not identifications. As we noted in GL15, the color shift induced by bulk motion is only a few tenths of a magnitude and is degenerate with normal giant-branch color evolution; the sky is full of Galactic dwarfs and unresolved background galaxies. An SHS is verified only when a velocity is measured: a grism radial velocity, a proper motion from Rubin or *Roman*, or both.

Figure 2 shows how the photometric counts depend on what is assumed. A shared space density would place the TP-AGB curve a factor ≈ 8 above the TRGB curve, the volume ratio implied by $\Delta M = 1.5$ mag in Figure 1(b). The two classes are not equally abundant. In GL15, red-giant-branch stars were about half of the detections at $H = 24$, with the shorter-lived, brighter giant branches contributing the rest. Matching that mix at $m = 24$ implies a TP-AGB space density lower by $(d_{\rm TP-AGB}/d_{\rm TRGB})^3 \approx 8$, so the Euclidean rises coincide: the extra volume and the lower density cancel. They peel apart only if each tracer is capped at $r_{\rm Virgo}$ (TP-AGB at $m_{\rm AB} \approx 25$, TRGB at ≈ 26.5), which we treat as a floor rather than the prediction. The shaded envelope is the eccentricity systematic alone, spanning $e_{12} = 0$ (a factor 1.7 below the fiducial) to $e_{12} = 0.9$ (a factor ≈ 6 above, the retrograde-disk channel of C. Tiede & D. J. D'Orazio 2024); it is not an error budget. A realistic photometric sample is of order 10^2–10^3. The kinematically verifiable subset is the nearby, brighter tail of that distribution.

We bound the same volume with two characteristic luminosities rather than the mixed isochrone sample of GL15. In GL15 we converted the kinematic population with stellar isochrones and a Kroupa IMF at an $H < 24$ (WFIRST- or Euclid-class) limit, without separating the tip of the red giant branch from the TP-AGB. We convert that mix into space densities so that the brighter class is not treated as equally numerous. Taking $M_{\rm AB} \simeq -4.5$ for the TRGB (M. J. B. Newman et al. 2024) and $M_{\rm AB} \simeq -6$ for luminous TP-AGB

[3] STScI *Roman* User Documentation, "High-Latitude Wide-Area Survey," https://roman-docs.stsci.edu/roman-community-defined-surveys/high-latitude-wide-area-survey, accessed 2026 August 29. Areas in the flight implementation are 2525, 2356, and 19.2 deg^2 for the wide, medium, and deep tiers; we round the first two in the text. The design origin is ROTAC.

stars (B. F. Madore & W. L. Freedman 2020), *Euclid* at $H = 24$ reaches 5.0 and 10 Mpc; HLWAS wide reaches 13.8 and 27.5 Mpc, and the deep tier 25 Mpc for the TRGB (Figure 1b). Both surveys detect evolved SHS throughout and well beyond the $r_{\rm Virgo} = 16$ Mpc volume within which GL15 computed the population; as argued above, that volume is a computational boundary rather than a physical one. Most of those detections will not have a measured velocity.

The sky distribution need not be isotropic. In GL15 the counts assumed an isotropic distribution, but we also noted that if mergers are plunging, the local population may originate from only a couple of events, and illustrated the case of a merger in M87 whose debris streams toward the Milky Way rather than filling the sky uniformly. The two deep-tier fields, COSMOS and XMM-LSS, lie 39° and 151° from M87; each sits inside one of the two medium-tier footprints. For stars streaming radially from $D = 16$ Mpc with a density falling as R^{-2}, the two carry weights of 1.9 and 0.35 relative to the all-sky mean. Because they lie on opposite sides of the sky the summed yield moves by less than 15%. The photometric rates above are therefore insensitive to whether the sources are isotropic or Virgo-dominated, even though the field-to-field split is not.

5.2. *Radial velocities: the grisms*

Both surveys disperse every source on the detector. At $R \sim 450$ (*Euclid*/NISP) to $R \approx 600$ (HLWAS), a bulk velocity of $10^4\,{\rm km\,s^{-1}}$ displaces spectral features by $\approx$ 15–20 resolution elements, $5000\,{\rm km\,s^{-1}}$ by $\approx$ 7.5–10, and $3000\,{\rm km\,s^{-1}}$ by $\approx$ 4.5–6. In slitless spectroscopy the wavelength zero-point is set by the source's position along the dispersion direction, so λ_0 requires astrometric registration to $\lesssim 1$ NISP pixel ($\approx 670\,{\rm km\,s^{-1}}$ at $R \sim 450$); that is why we lead with $10^4\,{\rm km\,s^{-1}}$, the velocity at which no competing channel operates. A stellar photospheric spectrum, with the CO bandheads near $1.6\,\mu$m and CN near $1.1\,\mu$m, is unmistakable against the smooth continuum of a background galaxy, and a *blueshifted* stellar spectrum has no astrophysical contaminant at all. That is a radial-velocity verification, obtained from the same exposures taken to measure galaxy Hα redshifts.

The continuum limit is the binding constraint, and it is where the two surveys trade area against depth. The published NISP 3.5σ continuum is $H = 19.5 \pm 0.2$ for compact galaxies (Euclid Collaboration & L. Gabarra 2023); NISP undersamples the PSF (0.″3 pixels), so that limit is already close to the point-source depth relevant for SHS. For HLWAS, the published one-hour point-source continuum limits at $1.5\,\mu$m are $m_{\rm AB} = 21.3$ (5σ per pixel) and 20.5 (10σ per pixel) (R. Akeson et al. 2019).[4] The medium-tier grism stack is 4 passes of 2×190 s dithers, or 1520 s on source. Scaling the 5σ per-pixel limit as $f_{\rm lim} \propto t^{-1/2} b^{1/2}$ gives $m_{\rm AB} \approx 20.8$ at the table zodiacal level and ≈ 20.9 at typical HLWAS backgrounds, confirming the $m_{\rm AB} \approx 21$ threshold adopted below.

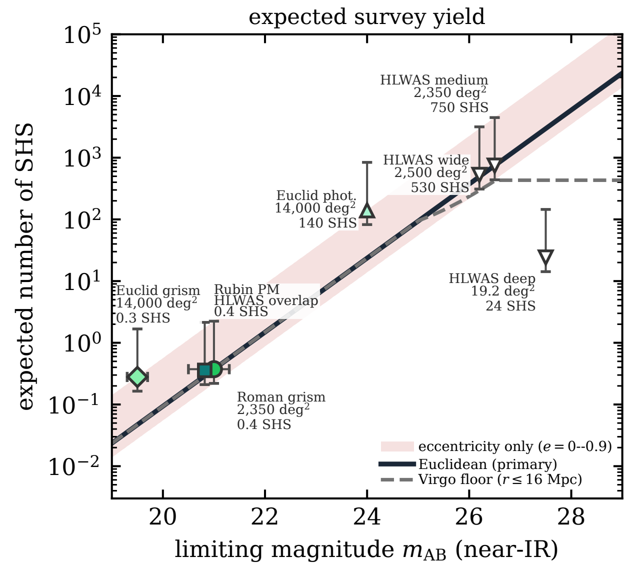

Figure 2. Expected number of SHS as a function of survey depth. The solid curve is Euclidean growth of the unboosted GL15 density (one SHS per 100 deg^2 at $H = 24$), the primary prediction; the dashed curve caps each tracer at $r_{\rm Virgo}$ and is a conservative floor. Green symbols are the *Euclid* and *Roman* cuts (Wide photometry and both grism continuum limits); the blue square is Rubin 5σ proper motions in r on the HLWAS footprint. Open symbols are the HLWAS photometric tiers. The Euclid grism bar is the published ±0.2 mag on $H = 19.5$. Grism markers sit at the published continuum depths; a velocity from bandheads is typically 0.5–1 mag brighter (see text). Vertical bars and the shaded band span the eccentricity systematic only, from $e_{12} = 0$ to $e_{12} = 0.9$; they are not a full error budget. Each survey is labeled with its name, area, and expected count.

The same surface density then gives both continuum yields (Figure 2). At $H = 19.5$, *Euclid* reaches 0.63 Mpc (TRGB) and 1.3 Mpc (TP-AGB); at $m_{\rm AB} \approx 21$, HLWAS reaches 1.3 and 2.5 Mpc. Counts scale as the cube of the

[4] NASA GSFC, "Wide Field Instrument Technical," https://roman.gsfc.nasa.gov/science/WFI_technical.html, and STScI *Roman* User Documentation, "WFI Quick Reference," https://roman-docs.stsci.edu, both give $m_{\rm AB} = 21.3$ (5σ per pixel) at $1.5\,\mu$m in 1 hr. R. Akeson et al. (2019) quote 20.5 at 10σ per pixel in the same time at $1.5\,\mu$m. Those tables assume twice the minimum zodiacal background; typical HLWAS backgrounds are $\sim$ 30% lower.

distance, and *Euclid*'s sixfold area (14,000 vs. 2350 $\deg^2$) only just cancels a ≈ 1.3 mag deficit, so the completed surveys yield ≈ 0.3 and ≈ 0.4 continuum detections at those published limits. A velocity from bandheads wants a signal-to-noise of a few per resolution element, typically 0.5–1 mag brighter, so the completed surveys yield of order 0.1–0.5 objects with a measured velocity, a few at $e_{12} = 0.9$. *Euclid*'s total is not yet in hand: it accumulates at $\approx 2300 \deg^2 \text{ yr}^{-1}$, the 5000 $\deg^2$ observed by 2026 March contain ≈ 0.1 expected continuum objects, and the $O(1)$ spectroscopic yield arrives when the Wide Survey finishes around 2030. HLWAS is slightly deeper and arrives later; its wide tier has no grism, so those ≈ 530 photometric detections are not spectroscopically verified by HLWAS itself.

These spectra are being taken regardless. A search for blueshifted stellar continua in the NISP or HLWAS grism requires no new observing time and no change to either observing strategy.

5.3. *Transverse velocities: Rubin and Roman astrometry*

HLWAS is not a proper-motion survey. Transverse velocities on its footprint come primarily from Rubin's decade-long baseline, with *Roman* supplying the NIR detection, a precise single-epoch position, and (in the medium and deep tiers) colors and, where bright enough, a grism spectrum. A star at $3000 \,\text{km}\,\text{s}^{-1}$ has a proper motion of 3.2, 1.3, and 0.63 mas yr^{-1} at 0.2, 0.5, and 1 Mpc respectively; at $10^4 \,\text{km}\,\text{s}^{-1}$ these become 10.5, 4.2, and 2.1 mas yr^{-1}.

Proper motion measures an angular rate; converting it to a transverse velocity requires a distance. A foreground M dwarf at 1 kpc moving at $5 \,\text{km}\,\text{s}^{-1}$ has $\mu \approx 1$ mas yr^{-1}, indistinguishable in μ alone from a $10^4 \,\text{km}\,\text{s}^{-1}$ star at 2 Mpc. A proper motion verifies an SHS only jointly: a TRGB- or TP-AGB-like SED in *Roman* colors, no measurable parallax, and a μ that is large *for a star at that photometric distance*, and only where *Roman* photometry exists.

The ten-year Rubin precision is $\sigma_\mu \approx 0.2$ mas yr^{-1} at $r = 21$ and ≈ 1.0 mas yr^{-1} at $r = 24$ (Ž. Ivezić et al. 2008, their Table 2). Cool giants are fainter in r than in F158; we adopt $r - \text{F158} \approx 1.5$ for the TRGB and ≈ 2.5 for TP-AGB and evaluate σ_μ at that r. Requiring a 5σ detection against the magnitude-dependent curve and applying the resulting distance cut consistently to both tracers confines the sample to 1.2 Mpc (TRGB) and 1.3 Mpc (TP-AGB) at $10^4 \,\text{km}\,\text{s}^{-1}$. Over the $\approx 4900 \deg^2$ HLWAS imaging area this yields ≈ 0.4 objects (Figure 2); over the full 18,000 $\deg^2$ LSST footprint (Ž. Ivezić et al. 2019), of order one. A Rubin-baseline plus *Roman*-epoch solution is in F158, where the star is bright, and may recover much of the previous reach. We quote the HLWAS overlap because only there do *Roman* colors supply the photometric distance. Objects detected only in F158 at $m_{\text{AB}} \gtrsim 24$ have no Rubin counterpart deep enough for that measurement. They remain photometric candidates.

The High-Latitude Time-Domain Survey (HLTDS) does supply an internal *Roman* astrometric baseline: repeat imaging over $\approx 18 \deg^2$ at a $\sim$ 5–10 day cadence for two years, with an extended component spanning the five-year mission (ROTAC). At $\sigma_\mu \approx 0.1$ mas yr^{-1} over that baseline a 5σ detection at $10^4 \,\text{km}\,\text{s}^{-1}$ reaches ≈ 4 Mpc and yields ≈ 0.06 expected SHS, comparable to the Rubin number on the HLWAS footprint rather than negligible. Any candidate that falls there will have a Roman-only proper motion, and the survey demonstrates that HLWAS need not be the last word on *Roman* astrometry.

A star with both a several-thousand $\text{km}\,\text{s}^{-1}$ blueshift and a proper motion large for its photometric distance, with no measurable parallax, is unambiguous. The grism alone still verifies against every astrophysical contaminant at $R \sim$ 450–600. The deep tier, observed in part early and in part later in the mission, may add a short *Roman*-only astrometric baseline on 19.2 $\deg^2$, useful for any candidates that fall there but not a survey.

5.4. *Contaminants*

Four populations will dominate a candidate list, and each is separable. Galactic halo dwarfs share the colors of distant giants but have radial velocities below the local escape speed ($\sim$ 500–600 $\text{km}\,\text{s}^{-1}$; T. Piffl et al. 2014) and large parallaxes or proper motions inconsistent with megaparsec distances. Unresolved background galaxies are redshifted and, at $R \sim$ 450–600, show no stellar photospheric features. Ordinary hypervelocity stars from the Galactic center or the LMC (W. R. Brown 2015; J. J. Han et al. 2025) have velocity vectors that trace back to those nuclei; SHS will not. In GL15 we showed that if ejections are beamed, several SHS would share trajectories pointing back to a common source galaxy, illustrated there with a merger in M87, a distinctive signature rather than a contaminant. Intracluster and intragroup giants, tidally stripped and bound to the cluster potential, have velocities of a few hundred to $\sim 10^3 \,\text{km}\,\text{s}^{-1}$ and cluster spatially around their hosts (A. Longobardi et al. 2015), whereas SHS are unbound and would stream radially from their source at several thousand $\text{km}\,\text{s}^{-1}$ or more.

6. DISCUSSION

Two related searches overlap this one. J.-H. Wang et al. (2025) have modeled "intergalactic wandering stars" within 10 Mpc produced by the Hills mechanism acting on the Galactic center MBH, predicting a few thousand objects detectable by Rubin and the China Space Station Telescope. Their population and ours are separated in velocity and origin (theirs peaks near $10^3\,\mathrm{km\,s^{-1}}$ and points back to the Galactic center, ours extends to $10^5\,\mathrm{km\,s^{-1}}$ and may point back toward Virgo), but any pipeline built to find isolated unbound stars will recover both. Separately, J. R. Martinez et al. (2022) showed that the bow shocks of semi-relativistic stars should produce detectable non-thermal radio emission, a channel that has not been used and that SKA-era surveys may make competitive with deep infrared imaging.

No candidate SHS has been identified, and none of the fast stars discovered in the interim is one: the current record holders among unbound stars are the $\approx$ 2000–2800 $\mathrm{km\,s^{-1}}$ survivors of double white dwarf detonations (K. El-Badry et al. 2023; R. Pakmor et al. 2026), an order of magnitude too slow and produced by thermonuclear rather than black hole physics. The star S301, announced in 2026 with a pericenter speed of $2.5\times10^4\,\mathrm{km\,s^{-1}}$ (GRAVITY Collaboration et al. 2026), is gravitationally bound to Sgr A* on an 8.7 yr orbit and is not an ejected star at all, though it may be the captured companion of the hypervelocity star S5-HVS1 (A. Caputo & G. M. Tomaselli 2026). If so, this would confirm Hills-mechanism physics at the level of an individual binary.

The spectroscopic search can begin with *Euclid* DR1 in 2026 October; the $O(1)$ Wide-Survey spectroscopic yield arrives around 2030, contemporaneous with the first HLWAS medium-tier grism fields. *Roman*'s deeper imaging then expands the photometric candidate list, and its slightly higher resolving power and fainter continuum limit expand the spectroscopic reach.

The HLWAS tiers do not arrive together, which bears on where a *Roman* photometric selection should start. Under the observing plan published before launch, the 19.2 deg^2 deep tier is to be completed by 2028 February, a half-depth pass of the ultra-deep tier follows in 2028 April–June, and the first medium-tier field, and thus the first grism spectroscopy, is to be completed by the end of 2028, while the wide tier receives only partial coverage within the first two years of science operations.[5] The deep tier is therefore where the *Roman* photometric selection should be developed: it exists first, it carries the most filters, and Euclidean growth puts $\approx$ 24 photometric detections there rather than a handful. Bulk selection is a giant-branch SED at giant luminosity, inconsistent with a dwarf sequence, using that filter set for luminosity-class leverage; at the extreme tail ($\beta \sim 0.3$) the same SED is anomalously blue (4000 K $\rightarrow\sim$ 5400 K), consistent with a Doppler-shifted cool-giant template (J. Guillochon & A. Loeb 2015, their §6.1). Its grism exposures are eight times longer than the medium tier's, which deepens galaxy emission-line spectra and gains about a magnitude on stellar continua, still far shallower than the imaging, so most photometric detections there have no radial velocity. The NISP grism is already the spectroscopic search; the medium-tier grism is its *Roman* counterpart. Rubin proper motions accumulate in parallel. The wide tier's larger photometric sample is a candidate list for those proper motions and for later spectroscopy, not a catalog of SHS. A blueshifted giant in those data would be a direct tracer of an eccentric MBH merger.

ACKNOWLEDGMENTS

This work was supported in part by the Black Hole Initiative, which is funded by JTF and GBMF. We thank the *Euclid* Consortium and the *Roman* project and community survey definition teams for making the Wide Survey and HLWAS parameters public. An initial research draft of this paper was written by Anthropic's AI assistant, Claude (Opus 5). All text that was not written by the authors was reviewed and approved by the authors, and all references have been verified.[6]

Software: astropy (Astropy Collaboration et al. 2022), matplotlib (J. D. Hunter 2007), numpy (S. van der Walt et al. 2011)

REFERENCES

[5] STScI *Roman* User Documentation, "Roman Observations in the First Two Years of Science Operations," https://roman-docs.stsci.edu. These windows follow from the 2026 August 30 launch and 90 days of commissioning, and will shift with the actual operations schedule.

[6] We post the LaTeX source and the scripts that produce Figures 1 and 2 at https://github.com/guillochon/shs-followup.

Agazie, G., Anumarlapudi, A., Archibald, A. M., et al. 2023a, ApJL, 951, L8, doi: 10.3847/2041-8213/acdac6

Agazie, G., Anumarlapudi, A., Archibald, A. M., et al. 2023b, ApJL, 952, L37, doi: 10.3847/2041-8213/ace18b

Akeson, R., Armus, L., Bachelet, E., et al. 2019, arXiv e-prints, arXiv:1902.05569, doi: 10.48550/arXiv.1902.05569

Astropy Collaboration, Price-Whelan, A. M., Lim, P. L., et al. 2022, ApJ, 935, 167, doi: 10.3847/1538-4357/ac7c74

Bardeen, J. M., Press, W. H., & Teukolsky, S. A. 1972, ApJ, 178, 347, doi: 10.1086/151796

Baumgardt, H., Gualandris, A., & Portegies Zwart, S. 2006, MNRAS, 372, 174, doi: 10.1111/j.1365-2966.2006.10818.x

Bray, E., Batkis, M., Chambers, V. J., et al. 2024, Journal of Astronomical Telescopes, Instruments, and Systems, 10, 014003, doi: 10.1117/1.JATIS.10.1.014003

Brown, W. R. 2015, ARA&A, 53, 15, doi: 10.1146/annurev-astro-082214-122230

Brown, W. R., Geller, M. J., Kenyon, S. J., & Kurtz, M. J. 2005, ApJL, 622, L33, doi: 10.1086/429378

Caputo, A., & Tomaselli, G. M. 2026, arXiv e-prints, arXiv:2607.22517, doi: 10.48550/arXiv.2607.22517

Chen, Y., Daniel, M., D'Orazio, D. J., et al. 2026, Nature Astronomy, 10, 554, doi: 10.1038/s41550-026-02782-0

El-Badry, K., Shen, K. J., Chandra, V., et al. 2023, The Open Journal of Astrophysics, 6, 28, doi: 10.21105/astro.2306.03914

Euclid Collaboration, & Gabarra, L. 2023, A&A, 676, A34, doi: 10.1051/0004-6361/202346177

Euclid Collaboration, & Mellier, Y. 2025, A&A, 697, A1, doi: 10.1051/0004-6361/202450810

Evans, F. A., Rasskazov, A., Remmelzwaal, A., et al. 2023, MNRAS, 525, 561, doi: 10.1093/mnras/stad2273

Ginsburg, I., Loeb, A., & Wegner, G. A. 2012, MNRAS, 423, 948, doi: 10.1111/j.1365-2966.2012.20930.x

GRAVITY Collaboration, Abd El Dayem, K., Abuter, R., et al. 2026, arXiv e-prints, arXiv:2607.12664, doi: 10.48550/arXiv.2607.12664

Guillochon, J., & Loeb, A. 2015, ApJ, 806, 124, doi: 10.1088/0004-637X/806/1/124

Han, J. J., El-Badry, K., Lucchini, S., et al. 2025, ApJ, 982, 188, doi: 10.3847/1538-4357/adb967

Hills, J. G. 1988, Nature, 331, 687, doi: 10.1038/331687a0

Hunter, J. D. 2007, Computing in Science and Engineering, 9, 90, doi: 10.1109/MCSE.2007.55

Ivezić, Ž., Monet, D. G., Bond, N., et al. 2008, in IAU Symposium, Vol. 248, A Giant Step: from Milli- to Micro-arcsecond Astrometry, ed. W. J. Jin, I. Platais, & M. A. C. Perryman, 537–543, doi: 10.1017/S1743921308020103

Ivezić, Ž., Kahn, S. M., Tyson, J. A., et al. 2019, ApJ, 873, 111, doi: 10.3847/1538-4357/ab042c

Iwasawa, M., An, S., Matsubayashi, T., Funato, Y., & Makino, J. 2011, ApJL, 731, L9, doi: 10.1088/2041-8205/731/1/L9

Khan, F. M., Preto, M., Berczik, P., et al. 2012, ApJ, 749, 147, doi: 10.1088/0004-637X/749/2/147

Koposov, S. E., Boubert, D., Li, T. S., et al. 2020, MNRAS, 491, 2465, doi: 10.1093/mnras/stz3081

Lai, D., & Muñoz, D. J. 2023, ARA&A, 61, 517, doi: 10.1146/annurev-astro-052622-022933

Loeb, A., & Guillochon, J. 2014, arXiv e-prints, arXiv:1411.5030, doi: 10.48550/arXiv.1411.5030

Longobardi, A., Arnaboldi, M., Gerhard, O., & Hanuschik, R. 2015, A&A, 579, A135, doi: 10.1051/0004-6361/201525773

Madore, B. F., & Freedman, W. L. 2020, ApJ, 899, 66, doi: 10.3847/1538-4357/aba045

Marchetti, T., Evans, F. A., & Rossi, E. M. 2022, MNRAS, 515, 767, doi: 10.1093/mnras/stac1777

Martinez, J. R., del Palacio, S., Bosch-Ramon, V., & Romero, G. E. 2022, A&A, 661, A102, doi: 10.1051/0004-6361/202142727

Muñoz, D. J., Miranda, R., & Lai, D. 2019, ApJ, 871, 84, doi: 10.3847/1538-4357/aaf867

Newman, M. J. B., McQuinn, K. B. W., Skillman, E. D., et al. 2024, ApJ, 966, 175, doi: 10.3847/1538-4357/ad306d

Pakmor, R., Shen, K. J., Bhat, A., et al. 2026, A&A, 706, A239, doi: 10.1051/0004-6361/202557670

Peters, P. C. 1964, Physical Review, 136, 1224, doi: 10.1103/PhysRev.136.B1224

Piffl, T., Scannapieco, C., Binney, J., et al. 2014, A&A, 562, A91, doi: 10.1051/0004-6361/201322531

Roman Observations Time Allocation Committee. 2025, arXiv e-prints, arXiv:2505.10574, doi: 10.48550/arXiv.2505.10574

Sari, R., Kobayashi, S., & Rossi, E. M. 2010, ApJ, 708, 605, doi: 10.1088/0004-637X/708/1/605

Sesana, A. 2010, ApJ, 719, 851, doi: 10.1088/0004-637X/719/1/851

Sesana, A., Haardt, F., & Madau, P. 2007, MNRAS, 379, L45, doi: 10.1111/j.1745-3933.2007.00331.x

Sherwin, B. D., Loeb, A., & O'Leary, R. M. 2008, MNRAS, 386, 1179, doi: 10.1111/j.1365-2966.2008.13097.x

Siwek, M., Weinberger, R., & Hernquist, L. 2023, MNRAS, 522, 2707, doi: 10.1093/mnras/stad1131

Tiede, C., & D'Orazio, D. J. 2024, MNRAS, 527, 6021, doi: 10.1093/mnras/stad3551 van der Walt, S., Colbert, S. C., & Varoquaux, G. 2011, Computing in Science and Engineering, 13, 22, doi: 10.1109/MCSE.2011.37

Verberne, S., Rossi, E. M., Koposov, S. E., et al. 2024, MNRAS, 533, 2747, doi: 10.1093/mnras/stae1888

Wang, J.-H., Xiang, M., & Liu, J.-F. 2025, ApJ, 990, 58, doi: 10.3847/1538-4357/adf8c8

Zrake, J., Tiede, C., MacFadyen, A., & Haiman, Z. 2021, ApJL, 909, L13, doi: 10.3847/2041-8213/abdd1c